Thalamocortical coupling and cortical E–I balance generate diverse anesthetic α-spindles for interpretable EEG decoding

François David[1,2,*,†], Christophe Sun[1,*], Pierre-Olivier Michel[1], Jérémie Sibille[2], Nathalie Rouach[2], and David Holcman[1,3,†]

[1]Group of Data Modeling, Computational Biology and Applied Mathematics, École Normale Supérieure–PSL, 75005 Paris, France
[2]Collège de France, 75005 Paris, France
[3] Churchill College, Visitor DAMPT University of Cambridge, Cambridge CB3 0DS, United Kingdom
[*]These authors contributed equally to this work.
[†]Correspondence and requests for materials should be addressed to holcman.david@gmail.com or francois.david@college-de-france.fr

December 26, 2025

Abstract

Anesthesia is a common clinical procedure, yet its hallmark EEG motifs—spindles oscillating in the broad alpha-range between 4 and 16 Hz—are not enough interpretable from the neuronal circuit perspective and for predictive medicine. To fill this gap, we investigate here the neuronal mechanisms and mathematical principles of brain spindles by recording and modeling large-scale thalamo-cortical neuronal ensembles in mice under anesthesia. We report irregular weakly synchronized firing of thalamic and cortical neurons associated with spindle patterns, indicating an emergent network rather than cellular dynamics. The consecutive loss of balance between the firing of excitatory and inhibitory cortical neurons and the increased firing fluctuations, together play in favor of larger spindle amplitude. In addition, the continuous range of spindle frequencies observed reflects a tight equilibrium of interactions between the thalamus and cortex. To create a possible numerical twin of this complex dynamics that could be used during clinical anesthesia, we built a computational model that comprises a reciprocally connected excitatory and inhibitory representation of cortical and thalamic networks driven by random fluctuations. The model parsimoniously explains the changes in spindle dynamics when increasing the anesthesia dose. This model thus links in vivo brain sub-network dynamics with EEG for the readout of anesthetized brain states.

Introduction

Electroencephalogram (EEG) recordings reveal spindle-shaped oscillatory events [1] that span different frequency bands (Fig. 1): for example, 1) the delta δ band (1-4Hz) are characterized during deep sleep, 2) the human alpha α band (8-12Hz), namely, are associated with loss of alertness [2, 3, 1] and anesthesia [4] and 3) the ripple frequency band -100 to 300 Hz- of the hippocampus characterizes memory replay [5]. Spindle presence is often associated with learning and memory, decreased attention, and a tendency to appear during "offline" states of the brain when a subject disconnects from the outside world and when the brain follows its inner dynamics, raising then the questions of their functions [6, 7]. As this is the key to several strongholds of health and cognitive disorders, here we investigate the mechanisms of emergence of spindles in the α-band in the particular case of anesthesia.

The rhythm of the α-band appears predominant under anesthetics such as gabaergic agonists, eg propofol and halogenic gas (studied here) and shares many dynamical features with the α observed during awake decreased attention, but also during sleep, making its characterization still uncertain from the strict EEG point of view. Although its activity is centered around 10 Hz in humans, its equivalent in mice can span between 4 Hz for light anesthesia [8, 9] and up to 16

Hz when it emerges from burst-suppressions associated with deep anesthesia [10]. Mechanically, some thalamic neurons could entrain layer 4 cortical neurons [11, 12], while the cortex could also sustain α-paced activity on its own [13]. The similarity between α observed under anesthesia and the α-rhythm observed in the occipital cortex during lower attention[14, 15] has not yet been resolved. However, phenomenologically and physiologically, a decrease in attention has much in common with the appearance of anesthesia, while α-spindles of anesthesia diverge more from their sleep equivalent, whose mechanisms are rather dependent on the specific firing mode of thalamic neurons [16, 17, 18]. Nevertheless, when anesthesia becomes more profound, the α spindles are interrupted by iso-electric suppressions[19], and emerging bouts of EEG activity have dynamics that cover the α-frequency band whose circuit mechanisms are not fully characterized[20].

The formal understanding of spindles in the alpha frequency band is based on models that reproduce certain features observed at the cellular level in ex vivo preparations [11], taking into account individual neuron membrane mechanisms [21, 22] or neuron population models [23] but still considering oscillator properties of neurons [24]. However, neuronal ensemble activity during the alpha-rhythm is little considered [25, 26], modeled neuronal activity is either too synchronized to be comparable to the level of the neuronal population or the essential statistics of waxing and waning envelope of the signal are not considered. Similarly, models that account for other types of oscillation in the frequency range α, such as sleep spindles [27], reflect some neuronal synchrony close to the hyper-synchrony seen in epilepsy. Alternatively, mean field models, which abstract the biophysical complexity and neuronal spike global arrangement [28] provide the opportunity to propose phenomenological models that can account more accurately on the overall emergence principles of spindles in the α-band. We chose this approach of modeling to capture the neuronal ensemble dynamics observed during spindle. Therefore, the principles of spindle emergence in the alpha-frequency band need to be established.

In order to disentangle the principles that govern the emergence of spindle oscillations in the α-frequency band of anesthetized mice, we characterized 1) their statistics such as their waxing and waning time intervals, 2) the simultaneous neuronal activity under different anesthesia levels and 3) inferred a generic model. We found that the emergence of α-spindles, their amplitude, and their frequency are based on principles identical to those of an excitatory and an inhibitory neuronal populations mutually connected driven by noise[29]. In fact, the change of the excitatory (E) and inhibitory (I) balance observed through the change of firing rate of the excitatory and inhibitory neuron population of the mouse cortex induced by an increased anesthesia dose, operates a shift of the balance toward excitation relative to inhibition amid an overall decrease of neuronal firing rate. The network driven by an outspoken excitation and some larger fluctuations generate larger spindles. However, the change in α-band frequency could only occur when two E-I networks were

connected, seemingly mimicking the thalamic and cortical E-I subnetworks. For the first time, a minimalist model can explain spindle dynamics in the full mouse α-frequency band and generalize it to experimental conditions where the anesthetic dose is changed and induces a spindle type mutation in the field of anesthesia.

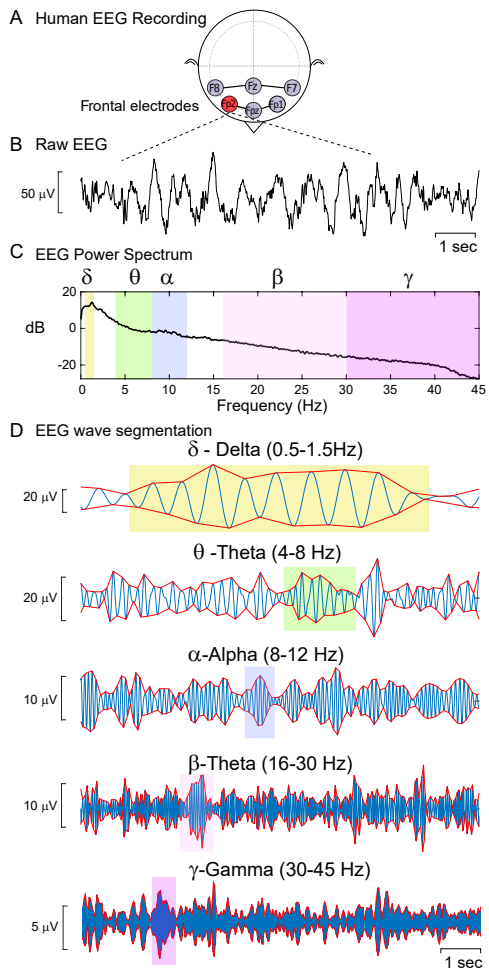

Figure 1: **Universal spindles across principal EEG frequency bands.** **(A)** Human clinical anesthesia EEG recording configuration. FP2-frontal electrode (red) used for the examples. **(B)** 10-second EEG sample. **(C)** Power spectral density of the raw sample EEG. Shaded regions correspond to the frequency bands - δ (0.5-1.5 Hz, yellow), θ (4-8 Hz, green), α (8-12 Hz, blue), β (16-30 Hz, red), γ (30-45 Hz, purple). **(D)** Filtered EEG traces (blue) and their envelopes (red) across frequency bands: δ, θ, α, β and γ. In each EEG frequency band, the activity can be decomposed and segmented in a succession of burst events (colored rectangles).

Results

Spike-train statistics of thalamic and cortical neurons during $\alpha-$spindles reveal Poisson-like distribution

To investigate how neuronal populations contribute to spindle dynamics, we recorded and analyzed the local field potential (LFP) in parallel to individual neuronal spikes (Fig. 2A-B). We first focus on $\alpha-$spindles (in the range of 4-16 Hz) of anesthetized mice, where the neuronal activity underlying LFP (Fig. 2 B) shows active firing with changing patterns in three neuronal populations: 1-excitatory thalamic neuronal axons (TC), 2-excitatory Regular spindles (RS) neurons, and 3- inhibitory cortical Fast spindles (FS) neurons (see methods for neuronal identification from extracellular spike shapes). The power spectrum of the LFP (Fig. 2C) shows a convex shape, suggesting a deviation from a power law EEG [6, 30].

To estimate the nature of neuronal activity in the absence of external stimulation, we investigated spike train variability and wondered whether their statistics would be random and thus approach a Poisson process. We report here that the distribution of the interspike interval (ISI) (Fig. 2 D) differs between inside (I) and outside (O) $\alpha-$spindles, measured by fitting the tail of the distribution, with an exponential rate $\lambda_I = 0.061s^{-1}$ (resp. $\lambda_O = 0.039s^{-1}$) for the RS, $\lambda_I = 0.059s^{-1}$ (resp. $\lambda_O = 0.038s^{-1}$) for the FS and $\lambda_I = 0.21s^{-1}$ (resp. $\lambda_O = 0.035s^{-1}$) for the TC. When considering the average over a population (n=4 mice) (Fig. 2E), we found that the distribution of the RS, FS and TC tail overlap both inside and outside $\alpha-$spindles. However, the TC distribution differs for short ISIs, as high-frequency bursts of action potentials are likely to increase during spindles [16]. Finally, to estimate the possible deviation (Fig. 2F) of these statistics from a Poisson process, we measure the number of spikes during time epochs and represent their mean vs. variance over 100 samples [31] when the time epoch is inside or outside the spindles. In both cases, the density distribution of the mean versus the variance differs from a pure Poisson process (diagonal : mean=variance) (Fig. 2F). However, the difference between inside and outside $\alpha-$spindles is almost null, suggesting that spike train statistics are closely related inside and outside of the $\alpha-$ spindles.

To conclude, spike distributions for both inside and outside spindles approach a random Poisson distribution well with distinct rates. However, these rates are quite comparable between FS and RS, and differ for the TC neurons.

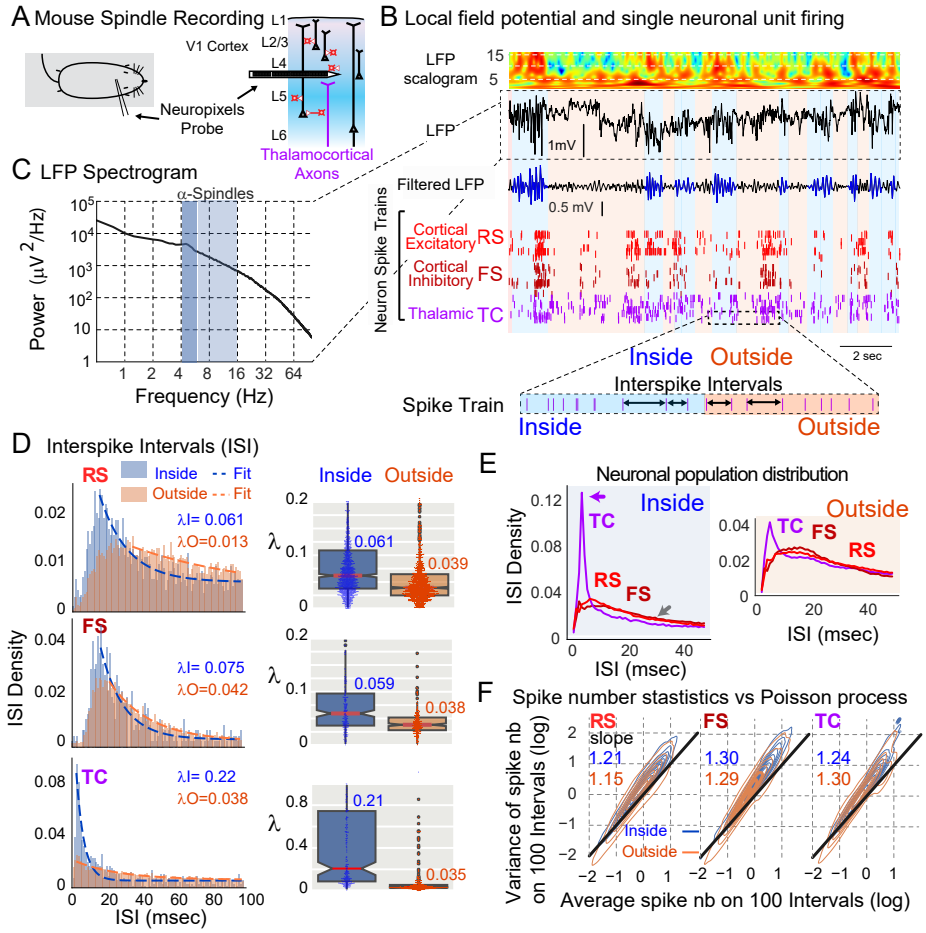

Figure 2: **Stochastic distribution of neuronal firing during $\alpha-$spindle dynamics (A)** Recording in anesthetized mice. The neuropixels electrode positioned in layer 4 of V1 cortex collect the local field potential (LFP) and extracellular action potentials of local cortical neurons and thalamocortical axons. **(B)** LFP scalogram (colormap), raw LFP (black), band-pass (6-16 Hz) filtered LFP overlaid by segmented spindles (blue). Spike time rasters of 20 excitatory cortical neurons (RS), inhibitory cortical neurons (FS) and 20 excitatory thalamic neuronal (TC) inside (overlaid in blue) and outside (orange) $\alpha-$ spindles. **(C)** LFP power spectrum. In dark and light blue, the $\alpha-$ low(4-6Hz) and high(6-16Hz)-frequency bands. **(D)** Left : Interspike Interval (ISI) density distributions for individual RS, FS and TC neurons inside (blue) and outside (orange) spindles. Dashed lines represent the fit with an exponential from the maximum of each distribution $a\exp(-\lambda t)$. Individual $\lambda-$ fit parameter value are indicated for inside and outside spindles (color code). Right: $\lambda-$ distribution (red : median, edges: quartiles,crosses: outliers) of the $\lambda-$ for each neuron (dots) inside and outside spindles. **(E)** Average ISI distribution density for the RS, FS and TC populations outside and inside the spindles (RS, n=1227, FS, n=228, TC, n=290). Note that the sharp peak at 2ms in TC distribution corresponds to high-frequency bursts of action potentials. **(F)** Density distribution (density lines) of variance versus mean number of spikes in 100 sequences taken inside (blue) and outside (orange) $\alpha-$ spindles for RS (slope=1.21 vs 1.15 inside and outside spindles respectively), FS (slope=1.30 vs 1.29) and TC (slope=1.24 vs 1.30). The two distributions distinguish from the diagonal (equivalent to a Poisson process (slope=1)) and between inside and outside spindles ($p<0.001$, Ancova test on the spindles).

Growth of E–I synchrony during α-spindle waxing and waning

To investigate the relation between individual spiking and the spindle dynamics, we explored here whether the spike trains would better align in time (i.e. be more synchronous with the LFP) as the spindles progress in time. We recall that spindles can be decomposed into a phase where the amplitude is increasing (resp. decreasing), called waxing (resp. waning), as shown in Fig. 3A-top), where the local minimum (troughs) are marked (round colored disks).

To estimate the spike-LFP alignment, we identified the LFP minima (Fig. 3 A-top), so that for each spike we could estimate the delay with respect to this reference, and the spike histogram can be compared when spikes are aligned with first, second, and third cycles from the beginning or from the end of the spindles(Fig. 3 A-left). We reported that for the three populations, large trough amplitudes are associated with an increase and anticipated population firing. However, we did not find any strong differences in firing between excitatory and inhibitory neurons in the waxing and waning phase (Fig. 3A-Right). At this stage, based on the synchrony of the inhibitory and excitatory neuronal population, we conclude that $\alpha-$ spindles could result from mutual interactions between inhibition and excitatory neurons, the population of which grows and becomes synchronized when the spindle amplitude increases (Fig. 3B). In addition, this process is driven by similar random noise (Fig. 2D-F). Thus, to account for these two features, 1-interacting excitatory and inhibitory populations and 2-spiking Poisson random noise, we propose an elementary computation model (Fig. 3C) based on recurrent interactions between excitatory and inhibitory populations [29].

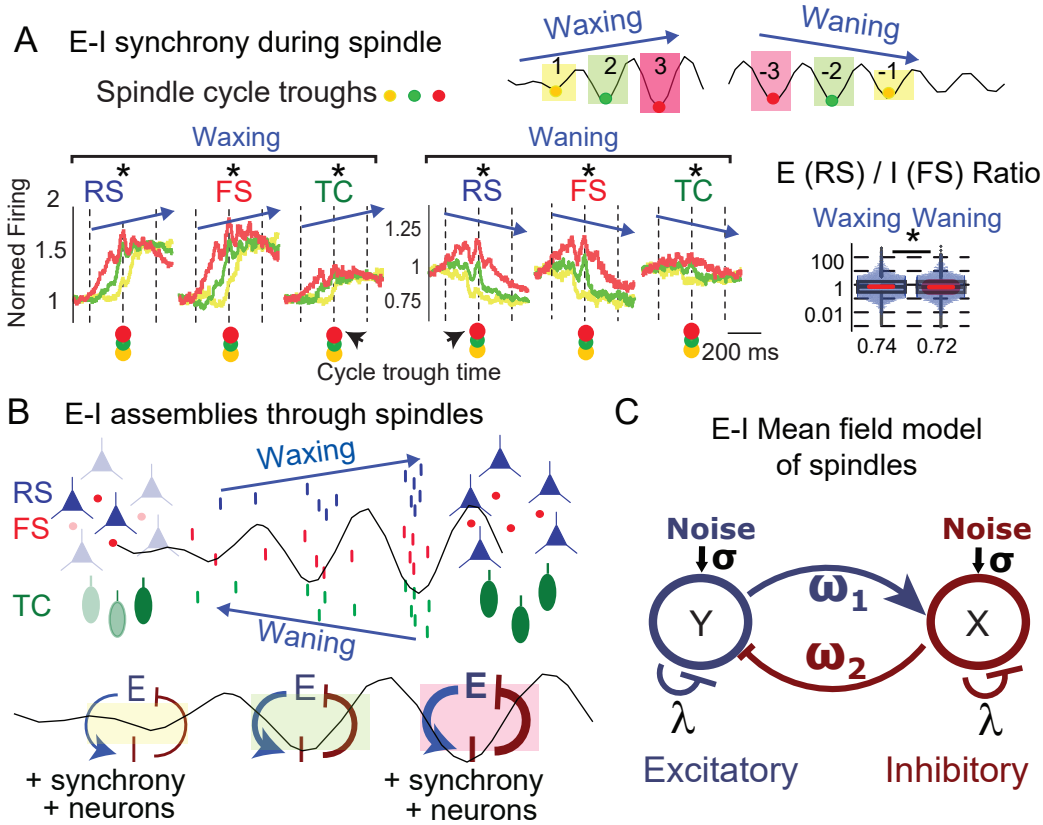

Figure 3: **Synchronous excitatory and inhibitory neuronal assemblies emerge with $\alpha-$spindle. (A)** Left: Comparison of neuronal synchrony in the first 3 and the last 3 spindle cycles for all types of neurons (RS, n = 1227, FS, n = 228, TC, n = 290). The firing histogram centered at each spindle cycle indicated synchrony increase, respectively decrease at the beginning (waxing) and end (waning) of the spindles. $*$ indicate significant difference ($p < 0.05$ w > 5000, Wilcoxon test) at time 0 msec between the 1st vs. 2nd and the 2nd vs. 3rd LFP troughs (color dots). Right : Firing ratio of RS (excitatory) and FS (inhibitory) neurons during waxing (left, mean 0.74) and waning (right, mean 0.72) significantly different ($p - val$<<0.01, Wilcoxon test, n=6190 spindles). **(B)** Population dynamics schematic of the thalamic and cortical network during the waxing and waning phase. As neurons fire more and are more synchronous when the spindle grows, the coupling strength increases. **(C)** These interactions can be modeled through a mean-field excitatory E and inhibitory I neuronal networks with direct ω_1, ω_2 and feedback -λ interactions driven by noise σ.

Stochastic E-I neural mass models generate spindle dynamics and define spindle statistics laws

To test the accuracy of the model, we first investigated whether random neuronal activity in a coupled E-I neuronal population is sufficient to generate spindles, and we implemented a reduced model that accounts for both neuronal populations driven by Brownian noise. In this model, the

excitatory population excites the inhibitory one with strength ω_1, while inhibiting itself with a decay rate λ, and the inhibitory network inhibits the excitatory network with strength ω_2, while also inhibiting itself with reciprocal connectivity (Fig. 3C). The equations are described in the method eq.2 .

Numerical simulations of the present model eq. 2 reveal the emergence of spontaneous transient spindles (Fig. 4A). The power spectrum of the spindles (Fig. 4A right) shows a single peak around the resonance frequency.

To characterize the spindle dynamics generated by the model, we segmented them (Fig. 4B, see methods) and extracted their statistical properties (duration, interspindle intervals, local maximum amplitude, waxing and waning duration and envelope values) (Fig. 4C-E, fig.1). Based on this segmentation, we collected spindle duration statistics that we fitted using the distribution $f_{\Delta}^{\lambda_{dur}}(t) = \lambda_{dur}^2 t \exp(-\lambda_{dur} t)$ (Fig. 4C left). Interestingly, the parameter λ_{dur} depends linearly on the parameter λ of the model (eq.) (Fig. 4C right), but remains independent of the noise amplitude σ (colored curved in Fig. 4C right). Similarly, the distribution of the interspindle duration is fitted by a single exponential with a decay rate λ_{inter} proportional to λ (Fig. 4D). Finally, the distribution of maximum amplitude of the filtered signal is fitted by $f_A^b(x) = \frac{x}{b^2} \exp\left(-\frac{x^2}{2b^2}\right)$ (see eq. 6) where $b = 4.3 \pm 0.2$ (Fig. 4E). The scale parameter b decreases with decay λ, but increases with the amplitude of noise σ. In summary, the spindles generated by the present stochastic model depend on the three parameters $(\lambda, \omega, \sigma)$, the individual spindles are random events and thus cannot be directly used to reflect the state of the E-I network so that the individual spindles may not carry any coding information about their generators on their own.

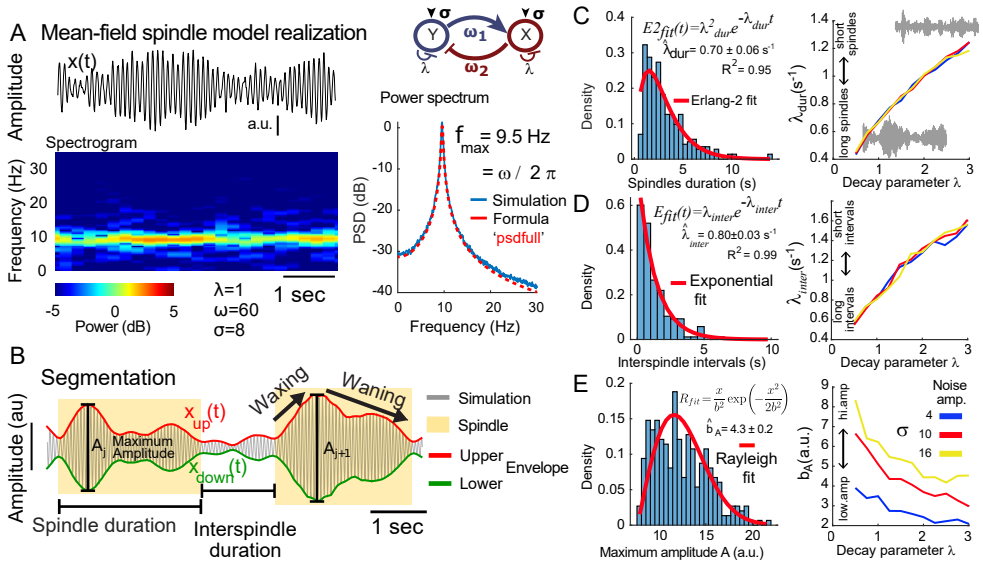

Figure 4: Spindles emerge from the stochastic process model with two interacting mean field populations. **(A)** First component $x(t)$ of a two-dimensional Ornstein-Uhlenbeck process (schematic) realization with parameters $\lambda = 1$, $\omega = 60$, $\sigma = 8$, its spectrogram (amplitude color coded), and it power spectrum density estimated from simulations (blue) and computed analytically (red) obtained in eq.(7). Amplitude of x is in arbitrary unit (a.u.) and $w = w_1 = w_2$ in equation 2. **(B)** Spindle segmentation from one realization of the model. **(C)** Left: Distribution of spindle durations over a 20-min simulation and its fit (red) using an Erlang-2 law (inset equation). Right: Evolution of the Erlang-2 parameter λ_{Erlang} with respect to the process decay parameter λ for different OU noise amplitude ($\sigma = 4, 10, 16$). Inset traces: 10 sec simulation with $\lambda = 0.5$ or $\lambda = 3$ and $\omega = 60$, $\sigma = 8$. **(D)** Left: Distribution of interspindle interval durations and its fit (red) using an exponential law (inset equation). Right: Evolution of the exponential decay parameter λ_{exp} with respect to the process decay parameter λ for different noise amplitude. **(E)** Left: Distribution of the spindle maximum amplitude A and its fit (red) using a Rayleigh law (inset equation). Right: Evolution of the Rayleigh scale b parameter with respect to the process decay parameter λ for different noise amplitude.

In vivo α-spindles obey the stochastic model statistics

To validate the model introduced above, we applied the same segmentation procedure and statistical analysis developed for the model to LFP in anesthetized mice for a low (Fig. 5A) and high anesthesia dose. For low doses, the dominant frequency is centered around $f = 5Hz$ (Fig. 5B-C). We used the Erlang2, respectively, exponential law to fit the spindle duration and, respectively, the interspindle duration, and obtained a good accuracy (Fig. 5D). Similarly, an exponential fit account for waxing and waning durations well (Fig. 5D right). The mean spindle duration was around $\bar{\tau}_{spindle} = 0.67$sec, the interspindle is $\bar{\tau}_{Interspindle} = 1.54$sec, while $\bar{\tau}_{Wanning} = 0.27$sec and $\bar{\tau}_{Waxing} = 0.26$sec (Fig. 5D). In addition, from the segmented spindles we obtained a mean frequency around 5.54 ± 0.94 Hz(Fig. 5E). Furthermore, the filtered signal maxima can also be

well fitted by a Rayleigh distribution (Fig. 5F) as predicted by the statistical laws that also characterize the model (Fig. 4E). In addition, during deep anesthesia spindle segmentation revealed different spectrograms enriched towards the 6-16 Hz band. Similarly to the low anesthesia dose, the duration of spindles, interspindle intervals, and waxing and waning were well fitted by the same laws. However, the spindle frequency distribution did not follow a Gaussian, and we found a deviation when studying the distribution of the local maxima amplitude of LFP. The deviation suggests either a heterogeneous spindle distribution or a different spindle generation mechanism. At this stage, we conclude that the present model statistics account well for the LFP spindles at 5Hz, with some deviation for those characterized by higher frequencies.

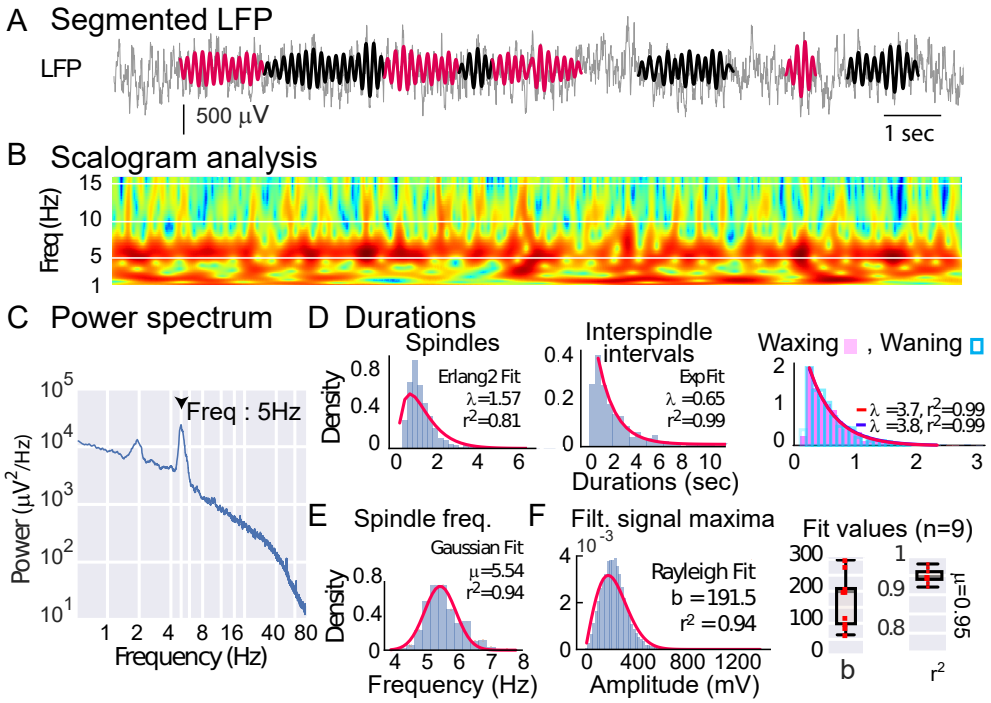

Figure 5: Spindles emerge in a narrow band of frequencies around 5 Hz at low anesthesia levels. **(A)** Raw LFP with segmented spindles (overlay alternating in red and black). **(B)** LFP scalogram showing a dominance of 5 Hz spindling activity). **(C)** Power spectrum of the LFP including the above sample. **(D)** Left: Distribution of spindle durations and its fit (red) using an Erlang-2 law. Middle: Distribution of interspindle durations and its fit (red) using an exponential law. Right: Distribution of the spindle waxing and waning durations. Fit values in the inset. **(E)** Distribution of spindle frequencies and its fit (red) using a normal law. **(F)** Left: Distribution of maximum amplitude A and its fit (red) using a Rayleigh law. Right: Rayleigh scale b and fit R^2 scatter and box plot indicate good fit performance for n=9 mice.

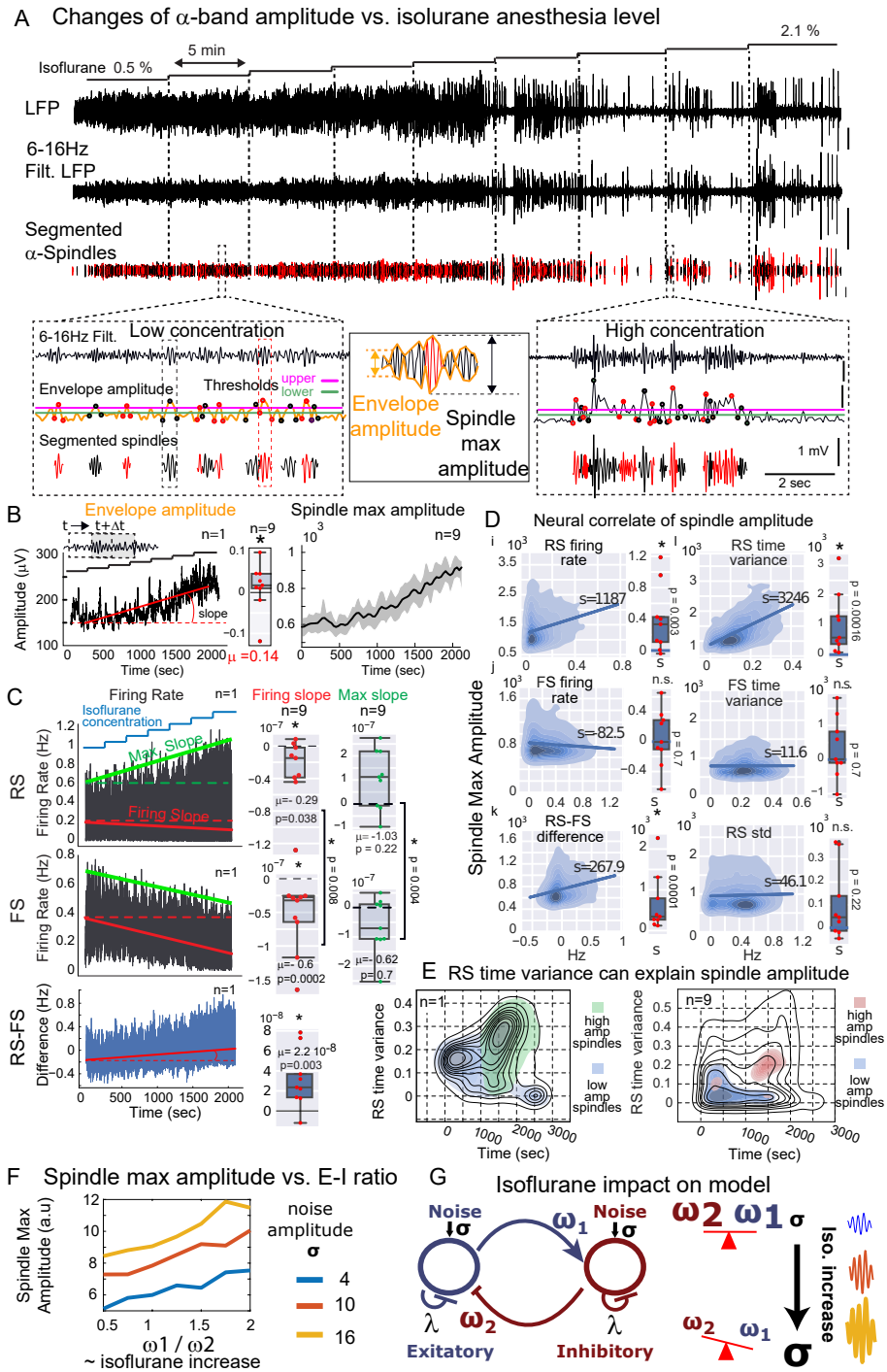

Figure 6: **Increasing anesthesia depth enhances α-spindle amplitude and shifts the excitation–inhibition balance. (A)** Experimental protocol: isoflurane concentration increased from 0.5% to 2.1% in 0.2% steps every 5 minutes. Top to bottom: (1) Raw local field potential (LFP) and (2) band-pass filtered LFP in the α band (4–16 Hz) show a progressive increase in oscillation amplitude; (3) Segmented spindles (waxing–waning events) identified by maxima of the envelope amplitude above an upper threshold (pink) flanked by two minima below a lower threshold (green). Insets illustrate the segmentation procedure at low (left) and high (right) isoflurane concentrations.

Figure 6 (continued). **(B)** Left: Mean envelope amplitude (n = 1 mouse) computed over a 100 s sliding window increases over time (red linear fit). Middle: Positive slope of the envelope amplitude over time is consistent across nine mice (Wilcoxon test, $p < 0.05$). Right: Mean spindle amplitude ± SEM (gray) (n = 9 mice) increases over the first 2100 s. **(C)** Example (left) and group data (right) for RS and FS firing rate (black) and their difference (blue). Linear fits of the firing rate and difference (red) show significant slopes (middle) as isoflurane increases (* indicate significative, Wilcoxon test, $p < 0.05$, n = 9). Linear fits of local maxima (computed on a sliding 100 s window) indicate opposite trends (green, left) and significantly different slopes between RS and FS (right, Wilcoxon test, $p < 0.05$, n = 9). **(D)** Density plots of spindle max amplitude (y-axis) vs. RS (i) and FS (j) firing rates, RS–FS firing rate difference (k), RS time variance computed between 0.5 s and the spindle max (l), same for FS (m) and firing variance across RS neurons (n). Box plots indicate the distribution of slopes for the n = 9 mice. * indicate statistical significance (Wilcoxon test). **(E)** Left: Density plots (lines) of spindle RS firing time variance as isoflurane increases over time (x-axis). The color code indicates spindles with highest and lowest amplitude quantiles ($q_{0.33}$ and $q_{0.66}$). Right: Same for all spindles from n = 9 mice. **(F)** Model output: α-spindle amplitude increases with both the excitation/inhibition ratio (x-axis) and noise amplitude (color coded), in agreement with experimental trends. **(G)** Model schematic illustrating how increasing isoflurane biases the excitation–inhibition balance toward excitation and can increase noise, resulting in an increase of spindle amplitude.

Deeper anesthesia boosts $\alpha-$spindle amplitude via an imbalanced E–I balance

To investigate how progressive increases in anesthesia dose influence α-spindle, we focus on changes in amplitude and the underlying excitation-inhibition balance (E–I) in cortical networks. In vivo LFP recordings were obtained in mice during stepwise increases in isoflurane concentration from 0.5% to 2.1% in steps of 0.2% every 5 minutes (Fig. 6A). Bandpass filtering in the $\alpha-$range (6–16 Hz) revealed a progressive increase in oscillatory amplitude (positive slope = $0.14\mu V/s$, $p < 0.05$, Wilcoxon test; Fig. 6B, left,fig:S3). Spindle events segmentation using our automated detection procedure (Fig. 6A, boxes) revealed larger-amplitude spindles at higher isoflurane concentrations, where the mean spindle amplitude, calculated in sliding windows of 100 s, increased over time in individual animals (Fig. 6B, right). Meanwhile, the firing rate of the neurons RS and FS recorded simultaneously decreases (Fig. 6C). However, refined characteristics of RS and FS indicated an increasing slope for RS maxima compared to decreasing for FS (Fig. 6C, green fit and right column). Moreover, the FS firing rate decreases more than for RS firing (Fig. 6C, red fit and middle column) as examined by computing the difference (Fig. 6C, bottom), indicating a gradual shift of the balance of E–I toward excitation. Based on the described impact of isoflurane concentration on E-I neuronal firing, our objective was then to directly correlate spindle amplitude with the firing rate properties of cortical neurons (Fig. 6D). RS firing and the difference in RS-FS firing (but not FS firing) were positively correlated with spindle amplitude (Fig. 6D, i-k). In addition,

the variance in the firing time of the RS (but not of the FS) firing also correlated positively with the spindle amplitude (Fig. 6B, l,m). However, the variance in RS firing across RS neurons was not correlated with spindle amplitude (Fig. 6D, n). Lastly, among the variables that were positively correlated with spindle amplitude, we found that the temporal variance of RS firing also increased, respectively, decreased, with the isoflurane concentration only for the highest, respectively, lowest amplitude part of the spindles (Fig. 6E). This suggests that the increase of spindle amplitude is driven by the proportion of spindles, which is associated with an increase in RS firing temporal fluctuations. In conclusion, we demonstrated here that the increase in spindle amplitude is driven 1) by the increase in RS and FS population differences and 2) by the increase in temporal fluctuations in cortical neurons. To interpret these findings, we used our computational model in which the spindle amplitude depends on the E–I ratio and the level of background noise. Interestingly, increasing the E–I ratio in the model reproduced the experimental increase in spindle amplitude (although the effect of the E-I ratio depends on the level of firing of E and I separately , Figs. 6F), and a further enhancement occurred when the noise amplitude was also increased (Fig. 6F). In conclusion, the present findings support the view that deepening anesthesia alters the E-I balance (Fig. 6G, changing the network toward increased excitatory dominance, thus affecting the α-oscillations and amplifying the spindle amplitude. This effect can be recapitulated in our model by differentially decreasing the weight coefficient ω_1 and ω_2, showing that the model can reproduce changes in the spindle amplitude.

$\alpha-$spindle frequency spectrum reflects the diversity of thalamo-cortical activation

In this section, we investigate the role of the thalamus and cortex in the genesis of spindle frequency. The model presented above suggested that the network connectivity is reflected in the spindle frequency and that the frequency varies with the amplitude similarly to the data. Thus, in this section, we decided to explore the extent to which the spindle frequency is controlled. First, from light to deep anesthesia, we observed an increase in the main spindle frequency from a narrow peak at 5Hz to a continuous 4 to 16Hz (Fig. 7A,B,S3). More specifically, the spindle frequency continuously increases with isoflurane concentration (slope=7 e^{-3}Hz.sec^{-1}, Fig. 7C). To dissect the contribution of the cortical and thalamic network, we decided to correlate the firing rate of RS and FS, and their difference (RS-FS) with the spindle frequency (Fig. 7D). Although there is a significant correlation with RS firing, this correlation would suggest a decrease in frequency as anesthesia deepens. In addition, there is no correlation with the difference in FS and RS-FS. Therefore, cortex activity does not play a direct role in spindle frequency changes. Based

on previous findings on the role of the thalamus in α-rhythmogenesis[12], we then investigated the role of the thalamus and found that a highly active thalamus is associated with a narrow frequency band of the spindles in the cortex, while little thalamic input to the cortex is associated with widespread α-spindle frequencies (Fig. 7E,F). In addition, we characterized the mode of firing of thalamic neurons. The bursting activity associated with the increase of firing mostly consists of high-threshold spike (low-frequency burst) and not low threshold spikes (high frequency bursts). To conclude, we found here that a strong thalamic input imposes a stereotyped 5-Hz α-frequency in the cortex, generated by RS-FS interactions, while a low thalamic input leads to high frequency α-spindles in the cortex. This suggests that the spindle frequency is possibly generated by network connectivity.

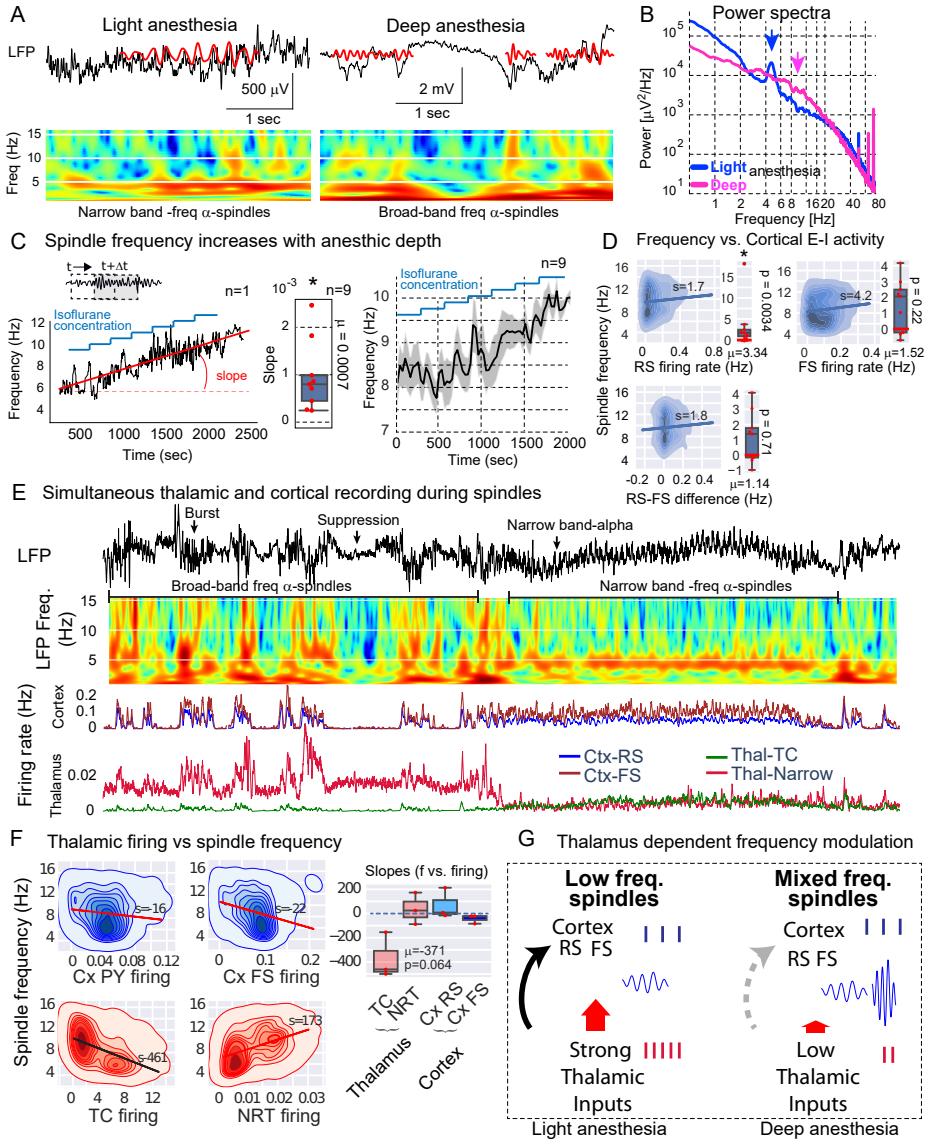

Figure 7: **Increasing anesthesia depth redistributes α-spindle frequencies and decouples thalamo-cortical inputs.** **(A)** Example of raw LFPs (black), segmented spindles (red) and scalograms (color maps) under light (left) and deep (right) anesthesia. **(B)** LFP power spectra under light and deep anesthesia show different deviations (arrows) from the tendency either as single peak at 5Hz or as a bulge from 3 to 16Hz. **(C)** Spindle frequency increases as the level of isoflurane increase (same protocole as in Fig.6A) on the example (left) and at the population level (middle and right, n=9, significant value for a Wilcoxon test). **(D)** Density plot examples of spindle frequency vs. RS firing rate (top,left), FS firing rate (top,right) and RS-FS firing rate difference (bottom) and box plots for population (n=9 mice) distribution. **(E)** Raw LFP with transition between deep anesthesia (with suppressions) and light anesthesia (Narrow band spindle). Below: average firing rate of the cortical RS anf FS populations during suppressions, mixed frequency spindles and low frequency. Note the contrasted thalamic activity between burst-suppression mode and narrow band alpha-spindles **(F)** Left : density of the spindle frequency vs. neuron firing rate for RS, FS, TC and NRT neurons. Right : Spindle frequency significantly correlate negatively with TC firing (n=3 mice). **(G)** Spindle frequency modulation schematics. High thalamic inputs (left) to the cortex result in low frequency spindles which low thalamic inputs (right) induce high frequency spindles.

Coupled thalamo-cortical neuron mass models reproduce anesthesia dose-dependent frequency shifts

To better understand that spindle frequency increases with anesthesia dose, we decided to use our modeling approach to account for thalamocortical interactions. For that goal, we coupled two stochastic focus models (Fig.8A) (see methods) and studied spindle dynamics in large and low coupling modes as a proxy of anesthetic concentrations (Fig.8B). Interestingly, the system generates spindles at the dominant frequency of 5 Hz when the coupling is high. In contrast, the system generates spindles at the dominant frequency of 7 Hz when the coupling is low. The coupled TC model can generate low- and high-frequency spindles as well as mixed spindles (mixture of high and low frequencies); therefore, we decided to study their proportion with respect to the properties of the coupling. When progressively increasing the coupling strength, we observe a decreasing proportion of fast in parallel to an increasing proportion of slow (Fig.8C) . At the transition, we report spindles with mix-frequency (red curve in (Fig.8C). Interestingly, when studying the order of spindle appearance in the coupling of two stochastic neuronal mass models, not necessarily reflecting thalamic-cortical interactions, high- and low-frequency spindles is random and could reflect the broad-band spindle frequency of spindles observed in the brain, with a continuum of spindle frequencies. To conclude, the present mass-model that accounts for thalamocortical interaction recapitulates the increase of spindle frequency while increasing the anesthesia dose.
To characterize the transition from low ($\tilde{5}$Hz) to mixed frequency α, we selected spontaneous transition events lasting 40 s, between these two spindle modes (Fig.8D): in this example, the LFP scalogram (Fig.8D-middle) shows a stable peak of frequency around a narrow-band during the first 20 s. This period is followed by another one, characterized by mixed frequencies. This transition (bifurcation between the two periods) is quantified in Fig.8D-lower panel based on a time-frequency segmentation applied on the scalogram (see Method). During the second period, multiple peaks are widely distributed around the narrow band α-frequency (Fig.8E-G). In conclusion, during anesthesia, the LFP shows multiple transitions from the mono-alpha band to multiple bands, reflecting dynamic transitions.

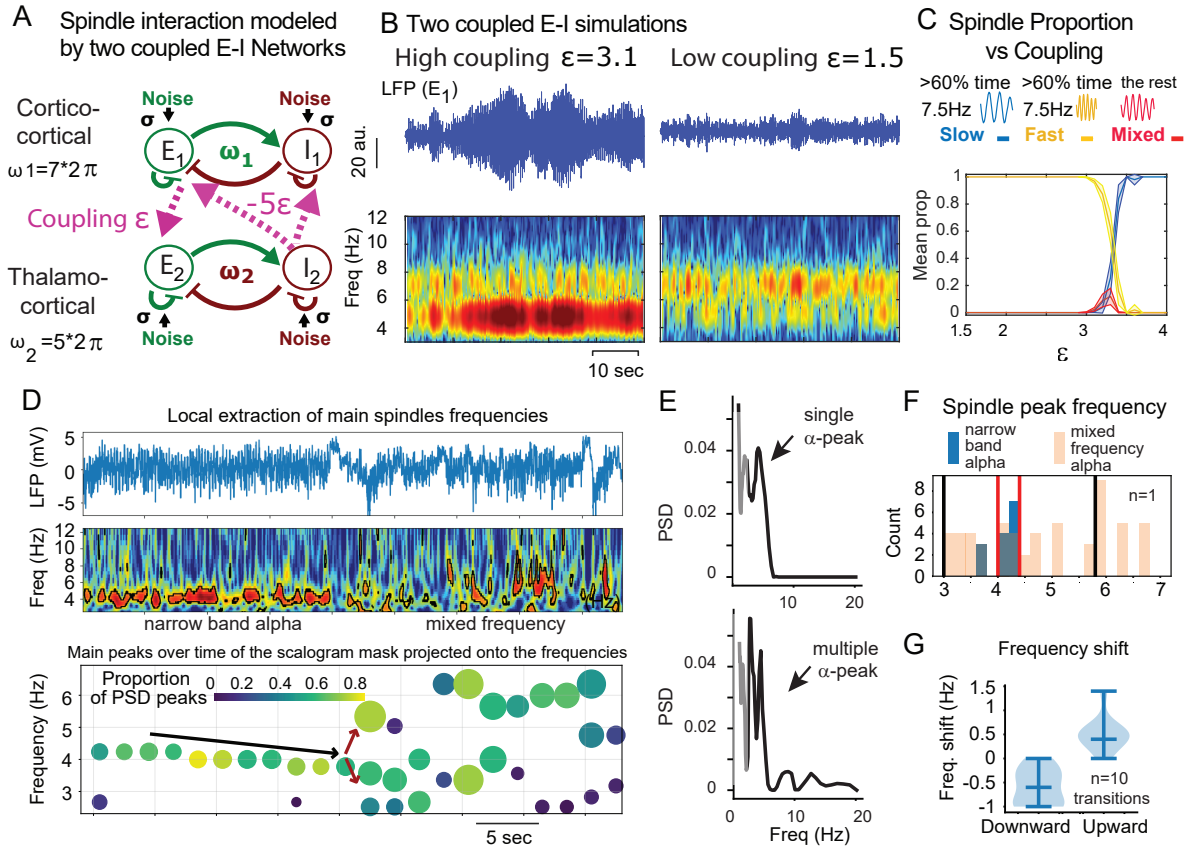

Figure 8: **Spindles of fast and slow frequencies reflect the coupling of 2 networks. (A)** Schematic model of two coupled E-I networks. ω_1=7*2π, ω_2=5*2π. λ=1 and σ=12. The coupling consists of ϵ with different factors as indicated in magenta. **(B)** Realization with ε=3.1 (left) and ϵ=1.5 (right) and the LFP spectrograms. **(C)** Evolution of spindle-type proportions with respect to the coupling strength ε indicate an progressive increase of slow spindle proportion compared to fast spindles when the coupling increases. **(D)** Top: LFP trace around the transition from narrow-band to mixed band alpha spindles. Middle : scalogram indicating time-frequency zones of maximal spindle intensity circled in black. Bottom: 4D plot indicating for each 2-sec time bin, the frequency of the power spectrum peaks (1,2 or 3 circles per time bin indicate multiple peaks, the proportion of the total PSD (color coded) and the amplitude of the peak (size coded). Arrows indicate a continuity during narrow band alpha and divergence during the mixed frequency alpha. **(E)** PSD of of the masked LFP during the narrow band alpha (top) and of the LFP during the mixed frequency alpha (bottom). Only the peaks between 2.5 and 20Hz are considered (black vs. gray). **(F)** Distribution of frequency peaks (from the example in (E)) before the bifurcation (blue) and after bifurcation (pink). Red and black lines indicate percentiles. **(G)** Averaged downward and upward deviations in Hz from the narrow band median frequency (n=10 bifurcations, n=4 mice).

Discussion

We combined here in vivo individual neuron and LFP recordings with neuronal-mass modeling to dissect the mechanisms that govern spindle dynamics during general anesthesia. We found that the amplitude and frequency of the α-spindle reflect the depth of brain sedation: higher amplitude spindles followed increased anesthesia (Fig. 6), along with an increase of the E-I imbalance, while the spindle frequency bifurcates with a reduced spindle frequency for those in continuity, but increases in the α-spindles present during burst-suppression (Fig. 7). In addition, we introduce a mass-neuronal model that can reproduce spindle statistics by accounting for the interaction between excitatory and inhibitory cortical neuronal populations. By coupling two- neuronal populations, the model further reproduces that a shift in the balance between inhibition and excitation toward excitation, amid a global decrease in neuronal activity, leads to the emergence of faster spindles when increasing the anesthesia dose (Fig. 8), thus accounting for the level of interaction between the cortex and the thalamus. The present framework offers a perspective on how spindles encode brain states and how they could be used to monitor sedation depth, more accurately than the dose of anesthesia.

Determinants of α-spindle frequency across species, age and anesthesia depth

The dominant frequency recorded in EEG during anesthesia varies between species of mammal, as illustrated for mice and humans or primates at 5Hz and 10Hz, respectively. This difference could question their functional link. However, both appear under light anesthesia [4, 8] or drowsiness [32, 7, 26]. They have the same frequency shift for these two conditions between species and are both associated with the spontaneous activity of the thalamocortical network [33, 26]. In fact, the 3-6 Hz-frequency band in mice has been described as a potential evolutionary precursor of α-activity [9] and μ-rhythms in rats [12].

The frequency of the α-band is also highly dependent on variables such as age, neurological conditions, or cognitive state [34]. The difference could be related to the properties of the inherent neuronal circuit such as the difference in the supra-granular layers of the cortex [35] essential for the α-rhythm [36] as they impact the specific resonance properties of the neocortex [37] or the large difference of the thalamic pulvinar nuclei between species [38] that proved essential for the gate of α[33] or even connectivity differences between humans and mice [39, 40].

When the concentration of the hypnotic drug increases, the spindle power is reduced, which could even lead to the loss of the alpha band (alpha-suppression) [41]. Interestingly, as isoflurane increases, we reported that the frequency of the α-spindle bifurcates into two asymmetric branches:

one characterized by low frequency and small power for the small spindle and the other with fast frequencies, present mostly during burst-suppression (Fig. 8D). This slowdown is similar to those of human studies, where the frequency of α typically decreases with increasing concentrations of volatile anesthetics [42].

Our modeling suggests that the decrease in spindle frequency can be linked to the decrease of synaptic connectivity strength whereas the increase in frequency associated with burst-suppression can be explained by changes in thalamocortical coupling (Fig. 7G,8): 1) When the cortical and thalamic networks are strongly coupled during light anesthesia, the spindle frequency is dominated by the slow mode 2) As anesthesia dose increases, the thalamic drive decreases, the cortical dynamics decouples, and higher frequency modes emerges in the cortex in burst-suppression α-spindles (Fig. 7). Thus, the increase in average frequency cannot be accounted for by local E/I cortical balance in the single focus model alone as it would predict a decrease in frequency, but instead reflects long-range thalamocortical interactions whose decrease alleviates some brakes on the cortical oscillators and allows higher frequency spindles. This interpretation is consistent with reports that anesthetics alter the excitability of thalamic relay cells and disrupt corticothalamic synchrony [43, 44]. It also suggests that beyond the classic thalamocortical system generating the low frequency alpha band, some other e i networks independent of the thalamus can emerge in the cortex and generate spindles at a broad range of frequencies. The number of those generators might not be limited to two as presented here (Fig. 8,S8). Surprisingly, the frequency functioning of these two modes is reminiscent of the multiple thalamus-dependent gamma frequency modes [45].

α-Spindle amplitude as a readout of E–I balance and firing variability

$\alpha-$Spindles were initially described as bursting events in thalamic and cortical neurons, driven by polarization of the resting membrane potential leading to activation of specific membrane ionic currents and electric synapses [46, 11]. Our experimental data showed here that the spindles emerge amid balanced cortical excitatory (RS) and inhibitory (FS) neuronal firing compared to firing outside the spindles (Fig. 2). However, the increase in spindle amplitude was associated with shifted excitatory-inhibitory ratios, across thousands of neurons recorded with Neuropixels probes (Fig.6C-D). Furthermore, increased variability in excitatory neurons firing also contributed to larger amplitude events (Fig.6D-E), suggesting that both the mean firing rate and the temporal dispersion of the spiking are critical determinants of the size of the spindle envelope (Fig.6F-G). When the thalamic inputs are strong (low frequency α associated with light anesthesia), the amplitude is small. These findings are consistent with the hypothesis that local thalamocortical and corticocortical interactions modulate the amplitude of the oscillation [11, 47, 48]. Importantly, our

mass neuronal model captures this effect: the amplitude increased with increasing noise amplitude (σ) and with a shift in the effective excitatory–inhibitory coupling. Thus, spindle amplitude can be interpreted as an emergent macroscopic readout of microscopic E/I network dynamics. This property also extends to sleep states, which are particularly sensitive to perturbations in homeostatic balance and can reveal latent hyper-excitability in vulnerable circuits, such as those observed in models of Alzheimer's disease [49, 50]. These findings also suggest that amplitude fluctuations during low-arousal states may directly reflect homeostatic E/I regulation.

Minimal population models of thalamo-cortical dynamics under anesthesia

Modeling thalamo-cortical rhythms in the 4 to 16 Hz range of activity serves to better characterize the mechanism of spindle genesis, but has faced two main challenges: 1) identifying the origins of rhythmic activity, in the thalamus or the cortex, and 2) identifying the initiation and termination mechanisms. Rhythmic activity depends on specific membrane channels, receptors, and synapses [21, 22], while initiation and termination could depend on adaptive currents [51] or short-term synaptic plasticity [52]. One caveat of the most recent models is the presence of very synchronized assemblies, which are far from normal physiological conditions, and the high number of parameters which cannot be entirely justified as most of them are not measurable. Previous modeling studies [53, 54, 55, 56, 57] have also shown that synaptic dynamics, especially involving short-term plasticity, can produce transient oscillations during cortical Up-states, where noise induces sustained bursts through stochastic resonance, while others proposed to describe such bursting activity, including mean-field or population-based neural field models [58, 59]. Instead, here, our model proposed a mechanism that kept minimal biological constraints and assumptions (Fig.4,6,7,S4,S5), i.e. includes excitatory and inhibitory populations, their synaptic connections, and some noise. In the second version (Fig.8,S8) the coupling of 2 similar networks to approximate the interactions of the thalamic and cortical circuits gives rise to spindles whose frequency depends on the coupling strength. The minimally constrained approach is flexible enough to be adapted to anesthetized mice and humans despite the large number of specie differences.

Leveraging spindle statistics for clinical anesthesia monitoring and prediction

Although spindles appear as stochastic realizations of a random system, where individual events are unpredictable, yet their statistics–duration, amplitude, and inter-spindle intervals–are tightly constrained by the model parameters. This paradigm shifts the emphasis from individual spindles

to their statistical evolution over time. The EEG spindle model in its simplest form (Fig. 4) could be used in real-time to monitor brain state stability provided the continuous estimation of only 3 parameters, thus providing a compact and physiologically interpretable representation of ongoing brain activity. In practice, this approach could enable the construction of a patient-specific numerical twin: a computational model that tracks the patient state stability based on the statistics of multiple spindles computed over hundreds of seconds. This framework could be used as a reference to quantify and predict the deviation that can be made at the single spindle level.

Current EEG-based indices, such as the bispectral index (BIS), rely on heuristic signal features that are not designed to predict the arrival of deep sedation characterized by burst suppression or excessive sedation [41, 60]. By contrast, tracking spindle statistics and their underlying parameters may allow predicting transitions to deep sedation before they occur [61]. In particular, inter-spindle intervals can provide an early signal to predict the arrival of burst suppression [62, 63, 64].

Anesthetic α-spindles reveal latent thalamo-cortical instabilities

Anesthesia could be used as a functional stress test to expose early circuit dysfunctions [50, 49]. In particular, in vulnerable states of neuro-degenerative diseases, such as Alzheimer's models [65, 49, 50], anesthesia challenges the E-I balance, even long before overt clinical symptoms appear. Indeed, while the healthy awake neocortex is dominated by inhibition [66], anesthesia reduces the balance between inhibition and excitation, thus creating particular conditions, which in the case where hidden dyshomeostatic network properties preexist, can create altered oscillatory dynamics. Thus, EEG quantification during anesthesia could provide early predictions of the brain degenerative route. The rate of change in spindle frequency and amplitude under anesthesia may reflect a principle of anesthetic-induced thalamocortical decoupling, a framework providing a quantitative model that links excitability shifts to measurable spindle statistics. Our modeling approach thus provides the formal tools to quantify such dysfunctions, by linking circuit-level instabilities to spindle statistics.

In summary, although we showed here that α-spindles during anesthesia can be mechanistically random patterns, shaped by cortical excitatory–inhibitory balance and thalamocortical coupling, their changes in amplitude and frequency could be used to assess the degree of brain sedation, while their statistical changes in time could offer predictive information about brain state transitions.

Material and Methods

Neuropixels Recordings

Mouse data were collected according to the requirements of the local ethics committee (APAFIS 50287-2024070300528714, agreement ID D750512). C57Bl6J 4- to 8-month-old mice, animals first underwent 1-% isoflurane anesthesia for cranial implantation. In the first two groups (n=4 and 9 mice respectively), a 384-channel Neuropixels 1.0 electrode was inserted into the primary visual cortex, parallel to layer 4, its position was confirmed by histology and by the presence of receptive fields in the neuronal activity observed in response to white squares on a black background visual stimulation. In the third group (n=3 mice), the electrode was vertically inserted (AP-2.5mm, ML:2mm, DV: 3.8mm) so that it crosses the visual cortex and thalamus The first group was maintained at a steady level of anesthesia with 0.7% isoflurane. The second group was under incremental anesthesia from 0.5% to 2.1% with 0.2 steps every 5 minutes (Fig.6). The anesthesia of the third group was constantly adjusted to capture the transitions from light to deep anesthesia. The recording procedures were similar to [67].

Spike train and local field potential pre-processing

Statistical analysis involved the use of Phy [68] and Kilosort [69] in a semi-automatic procedure. Briefly, spikes extracted from the high-pass full-band (30 kHz) signal were clustered according to the spike waveform and spatial location on the electrode.

Then based on well-characterized extracellular spike shapes of inhibitory neurons and excitatory neurons of the cortex and thalamus, spike waveforms with narrow spike shapes (trough-to-peak $< 0.5msec$) were classified as belonging to inhibitory cortical or thalamic neurons and those with broad spike shapes as excitatory cortical or thalamocortical neurons [70, 71].

Thalamocortical axons, which reflect thalamic neuron activity projected to layer 4 of the primary visual cortex, were identified based on the multi-phasic spike shape [67]. Spindles in the local field potential were segmented from the filtered signal. The signal envelope amplitude was estimated from the distance from inferior to superior envelope limits (see EMD for the detection of the envelopes) of the band-pass -6 to 16 Hz-filtered signal (unless noted differently). The amplitude maxima above an upper threshold (3 standard deviations) define the presence of a spindle. The minimum value of the nearest-in-time envelope inferior to a lower threshold (1.5 x std) and anterior, respectively, posterior, to the maximum is defined as the start, respectively, end of the spindle.

The variation in the envelope amplitude and spindle characteristics is only considered when they are outside suppressions detected based on the definition [41]. The local maxima of the histogram of each population firing are extracted over a sliding window of 100 seconds, and linearly fitted

to extract the slope (Fig. 6C). Power spectra were estimated using multi-taper analysis [72] for each 5-min interval corresponding to a particular dose of anesthetics. The values are averaged over a sliding window of 0.6Hz. The power spectrum ratios were calculated on these windowed values. The variables were compared using the Wilcoxon sign rank test (paired samples) or the Mann-Whitney U test (unpaired samples), as appropriate. The significance level used was α=0.05.

Spindle segmentation using the Empirical Mode Decomposition

We use the empirical mode decomposition [73, 74] (EMD), defined for a signal x as follows:

$$x(t) = \sum_{i=1}^{n} \mathrm{IMF}_i(t) + r_n(t) \tag{1}$$

where $\mathrm{IMF}_i(t)$ is the i-th intrinsic mode function and $r_n(t)$ is the residual after extracting n IMF [74, 75, 76]. In practice, we only use the first mode $n = 1$, allowing the identification of local extrema of $x(t)$ from the upper envelope $u(t)$ (resp. the lower envelope $l(t)$) (see Fig. 4A). We recall that $h_1(t) = f(t) - m(t)$, where $m(t) = \frac{u(t)+l(t)}{2}$.
The segmentation of spindles is obtained between two consecutive minima with a single global maximum. To obtain spindle segmentation, we use a first threshold $T_1 = \sigma$ (standard deviation of the signal) to extract the beginning and end of the spindles at $T_2 = 3\sigma$ to extract the maximum amplitude, so that there is only one large maximum per spindle. The lower threshold T_1 eliminates the possible fluctuation generated by the noise component of the amplitude. This procedure allows to segment the dynamics into spindles and periods in between, so that the max amplitude per spindle can be computed (Fig. 4B).

E-I model spectral properties

The model equation is given by

$$\begin{aligned} \dot{X} &= -\lambda X + \omega_1 Y + \sqrt{2\sigma_1}\dot{w}_1 \\ \dot{Y} &= -\omega_2 X - \lambda Y + \sqrt{2\sigma_1}\dot{w}_2 \end{aligned} \tag{2}$$

where $\boldsymbol{w}$ is the two-dimensional Brownian motion with mean zero. The oscillation is characterized by the two complex eigenvalues $\mu_\pm = -\lambda \pm i\omega$, where the main frequency is $\omega = \sqrt{\omega_1\omega_2}$. (The main frequency is $\omega/2\pi$). We consider here the case where the noise amplitude σ is neither too small nor too large (of the order 1) and the ratio $\frac{\omega}{\lambda} \gg 1$, a situation that differs from fluctuations

around a limit cycle oscillation, which is dominated by the deterministic component. Model 2 is a particular case of the Cowan-Wilson model [29] or can also result from the linearization of synaptic short-term plasticity mean-field model around the Up-state attractor [54, 77].
The steady-state distribution of the I-E dynamics is Gaussian [78, 79] in the variable $\boldsymbol{s} = (x, y)$

$$f(\boldsymbol{s}) = \frac{\lambda}{2\pi\sigma} \exp\left(-\frac{1}{2}\frac{\lambda|\boldsymbol{s}|^2}{\sigma}\right). \tag{3}$$

The distribution of spindle amplitudes is described by the equation for the radius $r = \sqrt{X_1^2 + X_2^2}$

$$dr = -W'(r)\mathrm{d}t + \sqrt{2\sigma}\mathrm{d}w. \tag{4}$$

where $W(r) = \frac{\lambda}{2}r^2 - \sigma\log(r)$. Thus, the noise amplitude has an equilibrium point at $W'(A_{asymp}) = 0$ defined by $A_{asymp} = \sqrt{\frac{\sigma}{\lambda}}$. The distribution of spindle amplitude is solution of the associated Forward Fokker-Planck equation

$$\begin{aligned} \frac{\partial}{\partial t}p(r,t) &= \frac{\partial}{\partial r}[W'(r)p(r,t)] + \sigma\frac{\partial^2}{\partial r^2}p(r,t) \\ p(r,0) &= \delta(r), \end{aligned} \tag{5}$$

where δ is the Dirac $\delta-$ function. The stationary solution ($\frac{\partial p}{\partial t} = 0$) is given by

$$p(r) = \frac{\lambda}{\sigma} r \exp\left(-\frac{\lambda}{2\sigma}r^2\right). \tag{6}$$

The power spectrum of the model equation is given by

$$\begin{aligned} S(f) &= \frac{1}{2\pi}\int_{\mathbb{R}} C_{xx}(\tau)\exp(-2i\pi f\tau)\,\mathrm{d}\tau \\ &= \frac{\sigma}{2\pi}\left(\frac{1}{\lambda^2 + (\omega - 2\pi f)^2} + \frac{1}{\lambda^2 + (\omega + 2\pi f)^2}\right), \end{aligned} \tag{7}$$

where C_{xx} is the autocorrelation function of the process first component [79]

$$\begin{aligned} C_{xx}(\tau) &= \mathbb{E}[(x(t) - \mu)(x(t-\tau) - \mu)] \\ &= \frac{\sigma}{\lambda}\exp(-\lambda|\tau|)\cos(\omega\tau). \end{aligned} \tag{8}$$

Coupled spindle generators eq. 9

We propose here to couple two spindle generators that correspond to two stochastic focus model with prescribed resonance frequencies $\omega_1 = 2\pi f_1$ and $\omega_2 = 2\pi f_2$. Specifically, the second system is coupled to the first by adding a small coupling parameter ϵ as follows:

$$\begin{aligned} \dot{X_1} &= -\lambda X_1 + \omega_1 Y_1 + \sqrt{2\sigma_1}\dot{w}_1 + \epsilon X_2 \\ \dot{Y_1} &= -\omega_1 X_1 - \lambda Y_1 + \sqrt{2\sigma_1}\dot{w}_2 \\ \dot{X_2} &= -\lambda X_2 + \omega_2 Y_2 + \sqrt{2\sigma_2}\dot{w}_3 \\ \dot{Y_2} &= -\omega_2 X_2 - \lambda Y_2 + \sqrt{2\sigma_2}\dot{w}_4, \end{aligned} \tag{9}$$

where w_i are Brownian motions and λ is the decaying parameter. The thalamocortical connectivity can be accounted for by several coupling parameters that we will introduce in the following system of equations where X_1, Y_1 can be associated to the cortex and X_2, Y_2 associated to the thalamus:

$$\begin{aligned} \dot{X_1} &= -\lambda X_1 + \omega_1 Y_1 + \sqrt{2\sigma_1}\dot{w}_1 - 5\epsilon Y_2 \\ \dot{Y_1} &= -\omega_1 X_1 - \lambda Y_1 + \sqrt{2\sigma_1}\dot{w}_2 - \epsilon Y_2 \\ \dot{X_2} &= -\lambda X_2 + \omega_2 Y_2 + \sqrt{2\sigma_2}\dot{w}_3 + \epsilon X_1 \\ \dot{Y_2} &= -\omega_2 X_2 - \lambda Y_2 + \sqrt{2\sigma_2}\dot{w}_4, \end{aligned} \tag{10}$$

Specifically, to account for the thalamocortical projections on the cortex, through a long-range excitatory connection, we added a coupling term $-\epsilon Y_2$ on the second variable Y_1 and a coupling term -5ϵ on the first variable X_1. To account for the cortico-thalamic projection on the thalamus, via a long-range excitatory connection, we added a coupling term $-\epsilon X_1$. The one hand from thalamocortical neuron axons projecting to inhibitory and excitatory neuron mostly from layer 4 of the cortex and 2) on the other hand from cortico-thalamic axons projecting from layer six pyramidal neurons to inhibitory reticular thalamic and thalamic neurons.

Measuring slow, fast and intermediate spindle sequence randomness using Wald Wolfowitz and Entropy

To evaluate the randomness of the three-valued spindle sequence (S, F, M), we use the Wald-Wolfowitz run test [80, 81]. A run is defined as a consecutive sequence of identical values. The null hypothesis H_0 assumes that the sequence is random. The number of runs under H0 can be

approximated by the expected number of runs given by the following expressions

$$\mathbb{E}(R) = \frac{2n_S n_F}{n} + \frac{2n_S n_M}{n} + \frac{2n_F n_M}{n} + 1 \tag{11}$$

where n_S, n_F, and n_M are the counts of slow, fast, and mixed spindles, and $n = n_A + n_B + n_C$ is the total number of spindles. The variance of the number of runs is calculated as

$$\mathrm{Var}(R) = \frac{2n_S n_F(2n_S n_F - n)}{n^2(n-1)} + \frac{2n_S n_M(2n_S n_M - n)}{n^2(n-1)} + \frac{2n_F n_M(2n_F n_M - n)}{n^2(n-1)}, \tag{12}$$

and the test statistic Z is

$$Z = \frac{R - E(R)}{\sqrt{\mathrm{Var}(R)}} \tag{13}$$

where R is the observed number of runs. The value of Z is compared to critical values from the standard normal distribution. If $|Z|$ exceeds the critical value 1.96 for $\alpha = 0.05$, H0 is rejected, indicating that the sequence is not random.

Bifurcation analysis on spectrogram

We describe here a method for segmenting spindles that could overlap in time, but can be resolved in the time-frequency domain, as they separate in their frequency (Fig. 8D). The method starts with building the scalogram using the complex Morlet wavelet (1.5-1.0). We then use a segmentation based on thresholding the upper 75th-percentile of the scalogram heatmap. The result provides clusters of high power spindles. In a second step, we further segment the long spindles, characterized by a number of pixels larger than the threshold $T = 20$ corresponding to the median value. This procedure provides a mask (only zero or 1) for the time-frequency spindle segmentation (black contour Fig.8D). To extract the spindles, we apply a sliding window of 5 s with 3 s overlap to get a time-bin histogram of the segmented frequency $F_t(f)$, which we normalize by the total integral $\frac{F_t(f)}{\int_{f>0} F_t(f)df}$ (Fig. 8E). Then, on each histogram, we detect each prominence peak above the arbitrary threshold 0.1 and their individual width (Fig. 8D bottom). Note that the larger the circle radius is, the wider is the peak.
We further develop an algorithm to segment the emergence of several spindle branches in the time-frequency domain. The scheme is described as follows:

1. Compute the distributions of the circles frequencies before and after a possible bifurcation.

2. Extract the proportion p_{before} of circles within a single narrow band frequency range $[f_0, f_1]$.

3. Compute the proportion p_{after} in the same frequency range $[f_0, f_1]$ as in the previous step, but now after a bifurcation has occurred (this proportion should be lower compared to the one computed before the bifurcation).

4. Identify the left and right bands to account for the same total power proportion as the band before bifurcation. To do so, we compute the upper frequency limit f_r so that the proportion in the band $[f_1, f_r]$ plus P_{after} is equal to $\frac{p_{before}}{2}$. We repeated a similar procedure to estimate the lower band f_l.

This procedure allows identifying two regions that contain each spindle branch after the bifurcation.

References

[1] Da Silva, F. L., Van Lierop, T., Schrijer, C. & Van Leeuwen, W. S. Organization of thalamic and cortical alpha rhythms: spectra and coherences. *Electroencephalography and clinical neurophysiology* **35**, 627–639 (1973).

[2] Berger, H. Über das elektroenkephalogramm des menschen. *Archiv für psychiatrie und nervenkrankheiten* **87**, 527–570 (1929).

[3] Davis, H., Davis, P. A., Loomis, A., Harvey, E. & Hobart, G. Human brain potentials during the onset of sleep. *Journal of Neurophysiology* **1**, 24–38 (1938).

[4] Purdon, P. L. *et al.* Electroencephalogram signatures of loss and recovery of consciousness from propofol. *Proceedings of the National Academy of Sciences* **110**, E1142–E1151 (2013).

[5] Girardeau, G. & Zugaro, M. Hippocampal ripples and memory consolidation. *Current opinion in neurobiology* **21**, 452–459 (2011).

[6] Buzsaki, G. *Rhythms of the Brain* (Oxford University Press, 2006).

[7] Jensen, O. Distractor inhibition by alpha oscillations is controlled by an indirect mechanism governed by goal-relevant information. *Communications Psychology* **2**, 36 (2024).

[8] Loison, V. *et al.* Mapping general anesthesia states based on electro-encephalogram transition phases. *NeuroImage* **285**, 120498 (2024).

[9] Senzai, Y., Fernandez-Ruiz, A. & Buzsáki, G. Layer-specific physiological features and interlaminar interactions in the primary visual cortex of the mouse. *Neuron* **101**, 500–513 (2019).

[10] You, Y. *et al.* Anesthetic spindles serve as eeg markers of the depth variations in anesthesia induced by multifarious general anesthetics in mouse experiments. *Frontiers in Pharmacology* **15**, 1474923 (2024).

[11] Hughes, S. W. *et al.* Synchronized oscillations at α and θ frequencies in the lateral geniculate nucleus. *Neuron* **42**, 253–268 (2004).

[12] Hughes, S. W. & Crunelli, V. Thalamic mechanisms of eeg alpha rhythms and their pathological implications. *The Neuroscientist* **11**, 357–372 (2005).

[13] Traub, R. D. *et al.* Layer 4 pyramidal neuron dendritic bursting underlies a post-stimulus visual cortical alpha rhythm. *Communications biology* **3**, 230 (2020).

[14] Başar, E. A review of alpha activity in integrative brain function: fundamental physiology, sensory coding, cognition and pathology. *International Journal of Psychophysiology* **86**, 1–24 (2012).

[15] Cimenser, A. *et al.* Tracking brain states under general anesthesia by using global coherence analysis. *Proceedings of the National Academy of Sciences* **108**, 8832–8837 (2011).

[16] Steriade, M. & Deschenes, M. The thalamus as a neuronal oscillator. *Brain Research Reviews* **8**, 1–63 (1984).

[17] De Gennaro, L. & Ferrara, M. Sleep spindles: an overview. *Sleep medicine reviews* **7**, 423–440 (2003).

[18] Fernandez, L. M. & Lüthi, A. Sleep spindles: mechanisms and functions. *Physiological reviews* **100**, 805–868 (2020).

[19] Altwegg-Boussac, T. *et al.* Cortical neurons and networks are dormant but fully responsive during isoelectric brain state. *Brain* **140**, 2381–2398 (2017).

[20] Yin, M. *et al.* Synchronicity of pyramidal neurones in the neocortex dominates isoflurane-induced burst suppression in mice. *British Journal of Anaesthesia* **134**, 1122–1133 (2025).

[21] Ching, S., Purdon, P. L., Vijayan, S., Kopell, N. J. & Brown, E. N. A neurophysiological–metabolic model for burst suppression. *Proceedings of the National Academy of Sciences* **109**, 3095–3100 (2012).

[22] Soplata, A. E. *et al.* Rapid thalamocortical network switching mediated by cortical synchronization underlies propofol-induced eeg signatures: a biophysical model. *Journal of Neurophysiology* **130**, 86–103 (2023).

[23] Bastiaens, S. P., Momi, D. & Griffiths, J. D. A comprehensive investigation of intracortical and corticothalamic models of the alpha rhythm. *PLOS Computational Biology* **21**, e1012926 (2025).

[24] Bhattacharya, B. S., Coyle, D. & Maguire, L. P. A thalamo–cortico–thalamic neural mass model to study alpha rhythms in alzheimer's disease. *Neural networks* **24**, 631–645 (2011).

[25] Lőrincz, M. L., Kékesi, K. A., Juhász, G., Crunelli, V. & Hughes, S. W. Temporal framing of thalamic relay-mode firing by phasic inhibition during the alpha rhythm. *Neuron* **63**, 683–696 (2009).

[26] Nestvogel, D. B. & McCormick, D. A. Visual thalamocortical mechanisms of waking state-dependent activity and alpha oscillations. *Neuron* **110**, 120–138 (2022).

[27] Destexhe, A. & Sejknowski, T. *Thalamocortical Assemblies: Sleep spindles, slow waves and epileptic discharges* (Oxford University Press, 2023).

[28] Sleigh, J., Voss, L., Steyn-Ross, M., Steyn-Ross, D. & Wilson, M. Modelling sleep and general anaesthesia. In *Sleep and anesthesia: neural correlates in theory and experiment*, 21–41 (Springer, 2011).

[29] Wilson, H. R. & Cowan, J. D. A mathematical theory of the functional dynamics of cortical and thalamic nervous tissue. *Kybernetik* **13**, 55–80 (1973).

[30] Dora, M., Jaffard, S. & Holcman, D. The wqn algorithm for eeg artifact removal in the absence of scale invariance. *IEEE Transactions on Signal Processing* (2024).

[31] Dayan, P. & Abbott, L. F. *Theoretical neuroscience: computational and mathematical modeling of neural systems* (MIT press, 2005).

[32] Crochet, S. & Petersen, C. C. Correlating whisker behavior with membrane potential in barrel cortex of awake mice. *Nature neuroscience* **9**, 608–610 (2006).

[33] Saalmann, Y. B., Pinsk, M. A., Wang, L., Li, X. & Kastner, S. The pulvinar regulates information transmission between cortical areas based on attention demands. *science* **337**, 753–756 (2012).

[34] Mierau, A., Klimesch, W. & Lefebvre, J. State-dependent alpha peak frequency shifts: Experimental evidence, potential mechanisms and functional implications. *neuroscience* **360**, 146–154 (2017).

[35] Kalmbach, B. E. *et al.* h-channels contribute to divergent intrinsic membrane properties of supragranular pyramidal neurons in human versus mouse cerebral cortex. *Neuron* **100**, 1194–1208 (2018).

[36] Halgren, M. *et al.* The generation and propagation of the human alpha rhythm. *Proceedings of the National Academy of Sciences* **116**, 23772–23782 (2019).

[37] David, F., Borel, M., Ayub, S., Ruther, P. & Gentet, L. J. Layer-specific stimulations of parvalbumin-positive cortical interneurons in mice entrain brain rhythms to different frequencies. *Cerebral Cortex* **33**, 8286–8299 (2023).

[38] Cortes, N., Ladret, H. J., Abbas-Farishta, R. & Casanova, C. The pulvinar as a hub of visual processing and cortical integration. *Trends in Neurosciences* **47**, 120–134 (2024).

[39] Campagnola, L. *et al.* Local connectivity and synaptic dynamics in mouse and human neocortex. *Science* **375**, eabj5861 (2022).

[40] Hunt, S. *et al.* Strong and reliable synaptic communication between pyramidal neurons in adult human cerebral cortex. *Cerebral Cortex* **33**, 2857–2878 (2023).

[41] Cartailler, J., Parutto, P., Touchard, C., Vallée, F. & Holcman, D. Alpha rhythm collapse predicts iso-electric suppressions during anesthesia. *Communications biology* **2**, 1–10 (2019).

[42] Hight, D., Voss, L. J., Garcia, P. S. & Sleigh, J. Changes in alpha frequency and power of the electroencephalogram during volatile-based general anesthesia. *Frontiers in Systems Neuroscience* **11**, 36 (2017).

[43] Ching, S., Cimenser, A., Purdon, P. L., Brown, E. N. & Kopell, N. J. Thalamocortical model for a propofol-induced α-rhythm associated with loss of consciousness. *Proceedings of the National Academy of Sciences* **107**, 22665–22670 (2010).

[44] Brown, E. N., Purdon, P. L. & Van Dort, C. J. General anesthesia and altered states of arousal: a systems neuroscience analysis. *Annual review of neuroscience* **34**, 601–628 (2011).

[45] Meyerolbersleben, L. S., Sirota, A. & Busse, L. Anatomically resolved oscillatory bursts reveal dynamic motifs of thalamocortical activity during naturalistic stimulus viewing. *Neuron* (2025).

[46] Patel, A. J. *et al.* Inhalational anesthetics activate two-pore-domain background k+ channels. *Nature neuroscience* **2**, 422–426 (1999).

[47] Fuentealba, P., Timofeev, I., Bazhenov, M., Sejnowski, T. J. & Steriade, M. Membrane bistability in thalamic reticular neurons during spindle oscillations. *Journal of neurophysiology* **93**, 294–304 (2005).

[48] Veit, J., Handy, G., Mossing, D. P., Doiron, B. & Adesnik, H. Cortical vip neurons locally control the gain but globally control the coherence of gamma band rhythms. *Neuron* **111**, 405–417 (2023).

[49] Zarhin, D. *et al.* Disrupted neural correlates of anesthesia and sleep reveal early circuit dysfunctions in alzheimer models. *Cell Reports* **38**, 110268 (2022).

[50] Slutsky, I. Linking activity dyshomeostasis and sleep disturbances in alzheimer disease. *Nature Reviews Neuroscience* **25**, 272–284 (2024).

[51] Lüthi, A. & McCormick, D. A. Periodicity of thalamic synchronized oscillations: the role of ca2+-mediated upregulation of ih. *Neuron* **20**, 553–563 (1998).

[52] Zonca, L. & Holcman, D. Emergence and fragmentation of the alpha-band driven by neuronal network dynamics. *PLoS Computational Biology* **17**, e1009639 (2021).

[53] Destexhe, A. Modelling corticothalamic feedback and the gating of the thalamus by the cerebral cortex. *Journal of Physiology-Paris* **94**, 391–410 (2000).

[54] Holcman, D. & Tsodyks, M. The emergence of up and down states in cortical networks. *PLoS computational biology* **2**, e23 (2006).

[55] Verechtchaguina, T., Sokolov, I. M. & Schimansky-Geier, L. First passage time densities in resonate-and-fire models. *Physical Review E—Statistical, Nonlinear, and Soft Matter Physics* **73**, 031108 (2006).

[56] Duc, K. D., Schuss, Z. & Holcman, D. Oscillatory decay of the survival probability of activated diffusion across a limit cycle. *Physical Review E* **89**, 030101 (2014).

[57] Dao Duc, K. *et al.* Synaptic dynamics and neuronal network connectivity are reflected in the distribution of times in up states. *Frontiers in Computational Neuroscience* **9**, 96 (2015).

[58] Brunel, N. Dynamics of sparsely connected networks of excitatory and inhibitory spiking neurons. *Journal of computational neuroscience* **8**, 183–208 (2000).

[59] Brunel, N. & Wang, X.-J. What determines the frequency of fast network oscillations with irregular neural discharges? i. synaptic dynamics and excitation-inhibition balance. *Journal of neurophysiology* **90**, 415–430 (2003).

[60] Shao, Y. R. *et al.* Low frontal alpha power is associated with the propensity for burst suppression: An electroencephalogram phenotype for a "vulnerable brain". *Anesthesia and analgesia* **131**, 1529 (2020).

[61] Sun, C. & Holcman, D. Combining transient statistical markers from the eeg signal to predict brain sensitivity to general anesthesia. *Biomedical Signal Processing and Control* **77**, 103713 (2022).

[62] Chemali, J., Ching, S., Purdon, P. L., Solt, K. & Brown, E. N. Burst suppression probability algorithms: state-space methods for tracking eeg burst suppression. *Journal of neural engineering* **10**, 056017 (2013).

[63] Plummer, G. S. *et al.* Electroencephalogram dynamics during general anesthesia predict the later incidence and duration of burst-suppression during cardiopulmonary bypass. *Clinical Neurophysiology* **130**, 55–60 (2019).

[64] Sleigh, J. W., Scheib, C. M. & Sanders, R. D. General anaesthesia and electroencephalographic spindles. *Trends in Anaesthesia and Critical Care* **1**, 263–269 (2011).

[65] Shoob, S. *et al.* Deep brain stimulation of thalamic nucleus reuniens promotes neuronal and cognitive resilience in an alzheimer's disease mouse model. *Nature Communications* **14**, 7002 (2023).

[66] Haider, B., Häusser, M. & Carandini, M. Inhibition dominates sensory responses in the awake cortex. *Nature* **493**, 97–100 (2013).

[67] Sibille, J., Gehr, C. & Kremkow, J. Efficient mapping of the thalamocortical monosynaptic connectivity in vivo by tangential insertions of high-density electrodes in the cortex. *Proceedings of the National Academy of Sciences* **121**, e2313048121 (2024).

[68] Rossant, C. *et al.* Spike sorting for large, dense electrode arrays. *Nature neuroscience* **19**, 634–641 (2016).

[69] Pachitariu, M., Steinmetz, N. A., Kadir, S. N., Carandini, M. & Harris, K. D. Fast and accurate spike sorting of high-channel count probes with kilosort. *Advances in neural information processing systems* **29** (2016).

[70] Barthó, P. *et al.* Characterization of neocortical principal cells and interneurons by network interactions and extracellular features. *Journal of neurophysiology* **92**, 600–608 (2004).

[71] McCafferty, C. *et al.* Cortical drive and thalamic feed-forward inhibition control thalamic output synchrony during absence seizures. *Nature neuroscience* **21**, 744–756 (2018).

[72] Gorgolewski, K. J. *et al.* Nipype: a flexible, lightweight and extensible neuroimaging data processing framework in Python. 0.12.0-rc1 (2016). URL http://dx.doi.org/10.5281/zenodo.50186.

[73] Jaffard, S., Meyer, Y. & Ryan, R. D. *Wavelets: tools for science and technology* (SIAM, 2001).

[74] Flandrin, P., Rilling, G. & Goncalves, P. Empirical mode decomposition as a filter bank. *IEEE signal processing letters* **11**, 112–114 (2004).

[75] Wu, Z. & Huang, N. E. Ensemble empirical mode decomposition: A noise-assisted data analysis method. *Advances in Adaptive Data Analysis* **1**, 1–41 (2009).

[76] Wu, H.-T. *et al.* An integrated complete ensemble empirical mode decomposition with adaptive noise to optimize lstm for significant wave height forecasting. *Journal of Marine Science and Engineering* **9**, 631–645 (2021).

[77] Zonca, L., Dossi, E., Rouach, N. & Holcman, D. Computational methods and algorithms to segment and model recurrent bursting events in long-time series springer nature book about neuromethods. In *New Aspects in Analyzing the Synaptic Organization of the Brain*, 323–370 (Springer, 2024).

[78] Risken, H. Fokker-planck equation. In *The Fokker-Planck Equation*, 63–95 (Springer, 1996).

[79] Schuss, Z. *Theory and applications of stochastic processes: an analytical approach*, vol. 170 (Springer Science & Business Media, 2009).

[80] Bradley, J. V. *Distribution-free statistical tests*, vol. 60 (United States Air Force, 1960).

[81] Sheskin, D. J. *Handbook of parametric and nonparametric statistical procedures* (Chapman and hall/CRC, 2003).